

Determination of fault planes in a complex aftershock sequence using two-dimensional slip inversion

Rachel E. Abercrombie,^{1,2,*} Stephen Bannister,¹ Aasha Pancha,¹ Terry H. Webb¹ and Jim J. Mori³

¹*Institute of Geological and Nuclear Sciences, PO Box 30368, Lower Hutt, New Zealand*

²*Department of Earth and Planetary Science, Harvard University, 20 Oxford Street, Cambridge, MA 02138, USA.*

E-mail: rachel@seismology.harvard.edu

³*Disaster Research Prevention Institute, Kyoto University, Gokasho, Uji, Kyoto 611-0011, Japan*

Accepted 2001 January 24. Received 2000 September 26; in original form 2000 February 14

SUMMARY

The (1994) Arthur's Pass earthquake (M_w 6.7, South Island, New Zealand) had a complex aftershock sequence including events aligned with major mapped faults. To determine whether the major NE–SW-trending strike-slip faults in the region were activated during this aftershock sequence, we investigate the largest well-recorded aftershocks. The Arthur's Pass earthquake itself was a reverse-faulting event, but the majority of the aftershocks were strike-slip. We use the empirical Green's function method to obtain source time functions for four aftershocks (M_L 4.1–5.1). We then invert for slip on each nodal plane and compare the variance reduction to determine which is the fault plane. The two largest earthquakes (M_L 5.1 and M_L 4.2) located close to the mapped trace of the Bruce fault both occurred on fault planes striking NNW–SSE, perpendicular to the strike of the Bruce and other regional strike-slip faults. The third earthquake studied (M_L 4.1), located on a lineation of aftershocks parallel to the regional mapped trend, had a preferred fault plane with a NE–SW strike. The fourth aftershock (M_L 4.1) was located close to the main-shock fault plane and had an oblique reverse mechanism. This earthquake exhibited northward directivity, but the fault plane could not be identified. The earthquake stress drops ranged from 1 to 10 MPa.

Key words: aftershocks, fault planes, New Zealand, slip inversion.

INTRODUCTION

The 1994 June 18 Arthur's Pass earthquake (M_w 6.7), which struck the central South Island of New Zealand, had a complex aftershock sequence (Abercrombie *et al.* 2000; Robinson & McGinty 2000). The earthquake was located about 25 km SE of the Alpine fault, which forms the boundary between the Australian and Pacific plates through the South Island (Fig. 1). The South Island is an area of oblique convergence, with plate motion partitioned between strike-slip and reverse faults (Anderson *et al.* 1993). NE–SW-trending strike-slip faults, including the Alpine and Harper faults, dominate the northern and central South Island (Fig. 1). The Arthur's Pass earthquake was a shallow (depth 5 km), primarily reverse-faulting event, striking NE–SW (Abercrombie *et al.* 2000). The aftershock sequence extends approximately 30 km SSE of the fault plane and is elongated perpendicular to the strike of the Bruce, Harper and other main mapped faults. Lineations of aftershocks also occur parallel to and aligned with these principal faults.

The majority of the aftershocks to the Arthur's Pass earthquake have strike-slip focal mechanisms, consistent with the regional stress field (Robinson & McGinty 2000). The nodal planes predominantly align parallel and perpendicular to the NE–SW-trending mapped faults. It is unclear whether significant slip occurred on the larger mapped faults (the Bruce and Harper faults, Fig. 1), or on unmapped conjugate faults.

The 14 largest aftershocks to the Arthur's Pass earthquake had $M_L > 5$ (Haines 1981), but 13 of them occurred before the portable stations were installed and so were poorly recorded. 11 of the largest aftershocks, including the largest (M_L 6.1), cluster at the southern end of the aftershock zone near the Harper fault (Fig. 1). One of the other three large aftershocks occurred NW of the main shock, one to the SW (near station WILA) and one near the mapped trace of the Bruce fault (M_L 5.1, Event A in Fig. 1). Regional and teleseismic data constrain the largest aftershocks to have principally strike-slip mechanisms consistent with rupture on the Harper fault or a conjugate fault (Abercrombie *et al.* 2000; Robinson & McGinty 2000). The fault

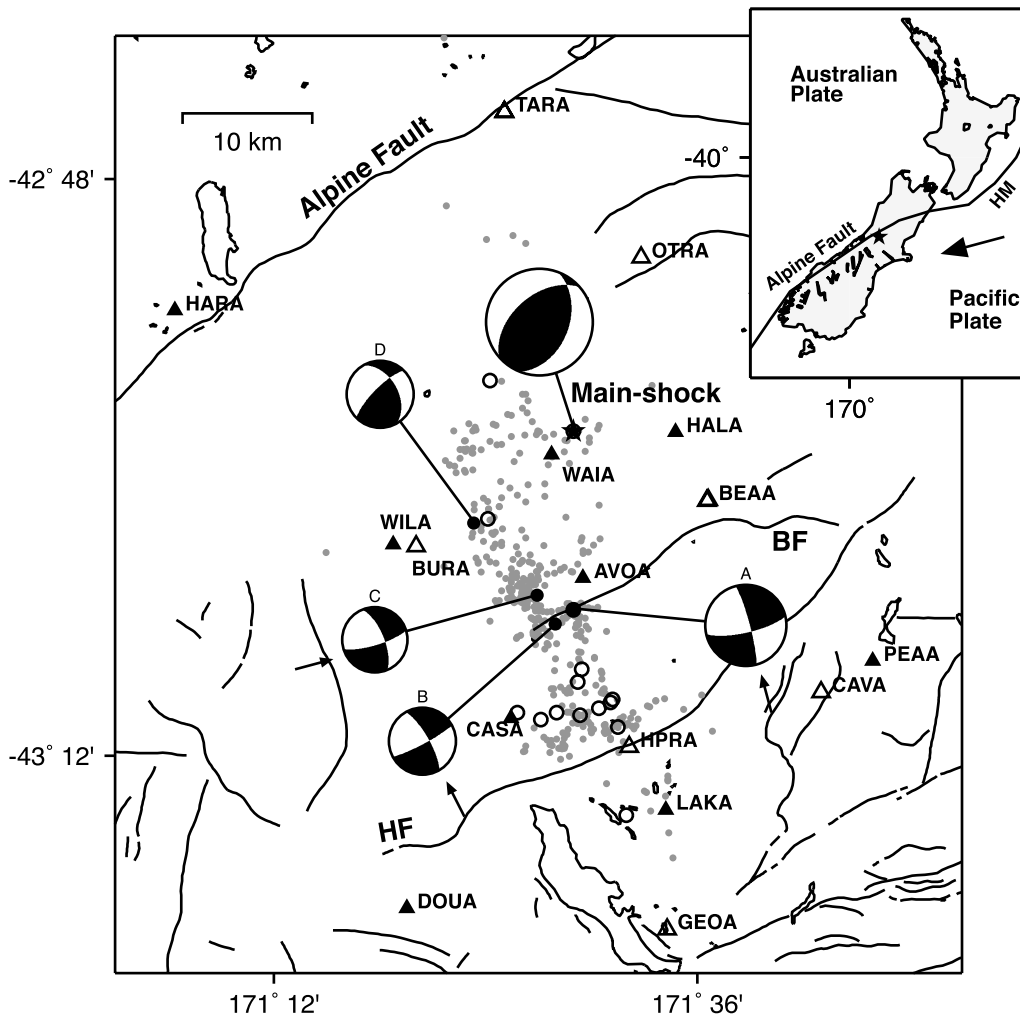


Figure 1. Map showing the location of the four earthquakes considered in this study (A–D, black circles). The Arthur's Pass main shock is shown by a star, and the best-located aftershocks as grey circles. The $M_L \geq 5$ aftershocks are plotted as open circles, except for Event A, which is included in this study. The major active faults are marked [BF = Bruce fault, as mapped by Chamberlain (1996) and HF = Harper fault]. The portable stations used to locate the aftershocks are shown as triangles and those also used in the slip inversion as solid triangles. The upper-hemisphere focal mechanisms of the Arthur's Pass main shock and the four aftershocks included in this study are shown; the arrows indicate the preferred fault plane in the slip inversions. The inset map shows the location of the Arthur's Pass main shock in New Zealand; the arrow indicates the motion of the Pacific plate relative to the Australian plate and HM is the Hikurangi margin.

planes cannot be distinguished from the regional short-period or strong-motion recordings. The aftershocks to the M_L 6.1 earthquake (1994 June 19; the most easterly of the lineation of $M_L \geq 5$ events extending from near station CASA) align roughly NNW–SSE, consistent with this largest (M_L 6.1) aftershock having ruptured a conjugate fault to the Harper fault (Abercrombie *et al.* 2000). The aftershocks to the M_L 5.7 earthquake (1994 June 21; the $M_L \geq 5$ aftershock nearest station HPRA) align roughly parallel to the Harper fault, suggesting that this (M_L 5.7) aftershock may have ruptured the Harper fault.

When the fault plane of a moderate-sized earthquake cannot be distinguished from the distribution of the aftershocks, the waveforms of the recorded seismograms can be used to determine the fault plane (e.g. Mori & Hartzell 1990; Mori 1993, 1996; Dreger *et al.* 1995). We use the procedure developed by Mori & Hartzell (1990) to determine the fault planes and source parameters of four well-recorded aftershocks of the Arthur's Pass earthquake.

The aims of the present study are to determine whether any of the larger mapped faults experienced significant seismic slip during the aftershock sequence, to confirm whether unmapped conjugate faults exist in the area, and to investigate whether aftershock lineations represent planes of significant slip. In addition, we obtain some of the first estimates of seismic moment and stress drop for moderate-sized New Zealand earthquakes.

DATA AND METHOD

The Arthur's Pass earthquake sequence was recorded by the New Zealand National Seismograph Network (NZNSN) of short-period (1 Hz, 100 sample s^{-1}) EARSS seismometers (Gledhill *et al.* 1991). 16 portable seismometers of the same type were installed in the five days following the main shock. The aftershocks were relocated using NZNSN and portable recordings and a 3-D velocity structure derived from inversion of the best-recorded events (Abercrombie *et al.* 2000). 10 $M_L \geq 4$

earthquakes occurred during the period of the portable deployment and were located with standard errors of ≤ 0.5 km horizontally and ≤ 1 km in depth.

Mori & Hartzell (1990) developed a two-step procedure to determine the fault plane from the recorded seismograms. First the site and path effects are removed from the seismograms of the earthquake of interest (main shock) using empirical Green's functions derived from the recordings of a relatively small, collocated earthquake. The resulting source time functions are then inverted for slip on each nodal plane of the focal mechanism to determine which matches these data better.

We searched the catalogue of well-located aftershocks for potential empirical Green's function events for the 10 well-recorded earthquakes. We required the empirical Green's function earthquakes to be well located, to be at least an order of magnitude smaller than their respective main shocks, and to be located within 2 km horizontally and 3 km in depth. We found candidates for four of the larger earthquakes, which we designate A, B, C and D, listed in Table 1 and plotted in Fig. 1. Both Events A and D had a second potential empirical Green's function earthquake, but the resulting deconvolutions were noisy, so we did not use them in the inversions. The focal mechanisms of Events A, B, C and D and their empirical Green's functions are well constrained, using both first motions and also amplitude envelopes of the *PS* waves (Robinson & McGinty 2000).

The four aftershocks that we are able to study include the only aftershock with $M_L \geq 5$ that was recorded by the portable network, on June 29 (M_L 5.1, Event A, Table 1 and Fig. 1). This aftershock was the largest to occur near the mapped active trace of the Bruce fault during the entire aftershock sequence. The second earthquake that we study (B, M_L 4.2) is also located close to the trace of the Bruce fault, and Event C (M_L 4.1) is located in a parallel-striking lineation of aftershocks to the north (Abercrombie *et al.* 2000). Both of these earthquakes have similar strike-slip mechanisms to Event A. The fourth earthquake (D, M_L 4.1) is located further north, near the inferred western termination of the main-shock rupture. Event D has a more oblique focal mechanism and a significant component of reverse motion, in common with many aftershocks near the main-shock fault plane (Robinson & McGinty 2000). Event D is also located close to the first M_L 5.1 aftershock that occurred 15 min after the main shock. This first M_L 5.1 aftershock was too poorly recorded to determine a focal mechanism.

To determine the source time functions of Events A–D, the seismograms of the small earthquakes (empirical Green's

functions) are deconvolved from those of their respective main shocks following the procedure described by Mori (1993, 1996). At all available stations, a time window between 3 and 4 s long, centred on the main-shock *P* or *S* waves, is chosen to include the principal arrivals. The vertical-component seismograms are used for the *P* waves and the two horizontal components are rotated to produce *SH*. The input waveforms for Event B are shown as an example in Fig. 2. We then deconvolve the empirical Green's function from the main-event seismogram by spectral division. Deconvolutions are calculated for all available stations and data, including *S* waves, but some of the deconvolved waveforms have low signal-to-noise ratios. Noisy data are dropped from the subsequent slip inversion so as not to degrade the stability of the inversion. The resulting source time functions, which we use in the inversions, are shown in Figs 3–6.

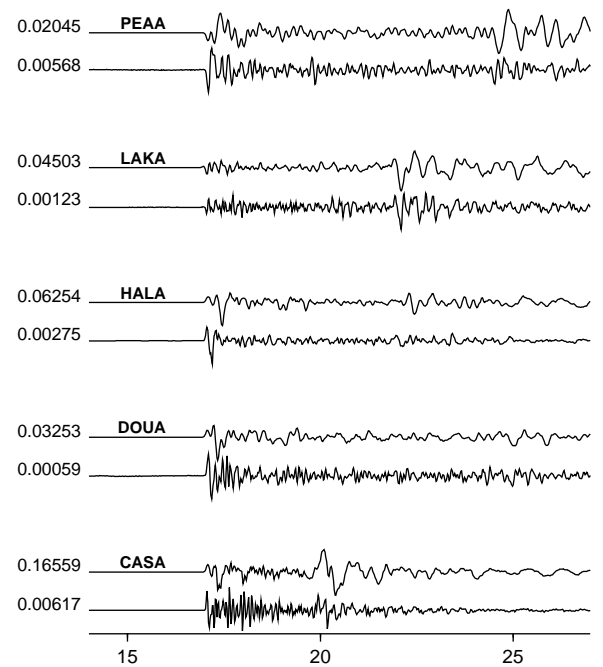


Figure 2. The vertical velocity seismograms for Event B (upper trace of each pair) and its empirical Green's function event (lower traces). They are aligned on the *P* wave, and the maximum amplitudes are given in cm s^{-1} .

Table 1. Hypocentre parameters of the four earthquakes and their respective empirical Green's function events.

Event	Date	Time (UT)	Lat. (°)	Long. (°)	Depth (km)	M_L	Strike (°)	Dip (°)	Rake (°)
A	29/6/94	5:38	-43.0985	171.4825	9.8	5.1	165	83	-15
	27/6/94	8:16	-43.0983	171.4823	10.1	2.8	157	83	-30
B	25/6/94	1:39	-43.1087	171.4660	5.5	4.2	150	75	-8
	22/6/94	13:37	-43.1087	171.4660	6.3	2.8	150	70	-22
C	26/6/94	11:06	-43.0890	171.4487	4.1	4.1	253	76	203
	24/6/94	16:10	-43.0890	171.4487	3.8	2.4	75	90	158
D	26/6/94	18:12	-43.0387	171.3887	9.1	4.1	45	75	135
	26/6/94	16:27	-43.0442	171.4018	8.0	2.4	45	60	135

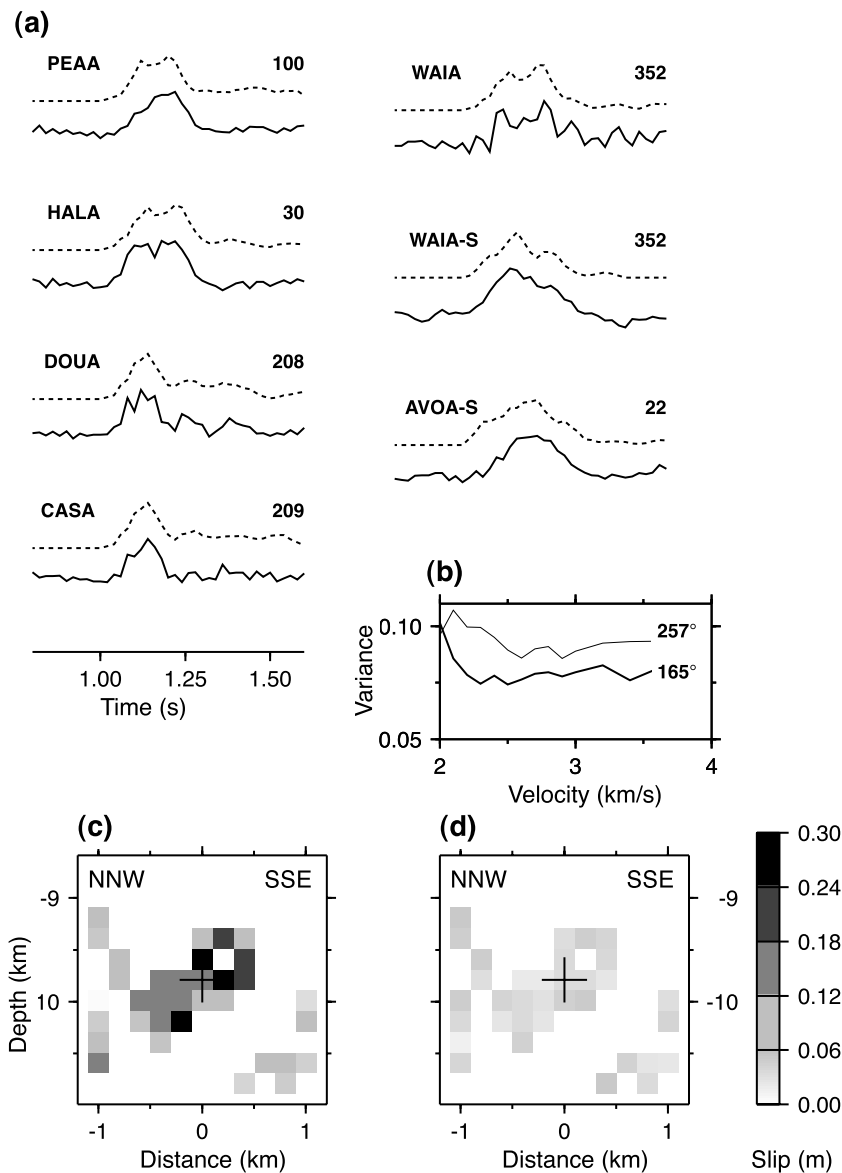


Figure 3. Event A (M_L 5.1): source time functions and slip inversion results. (a) Deconvolved source time functions input to the slip inversion (solid lines) and the synthetic seismograms from the best-fitting model (dashed lines) using the 165° plane and a rupture velocity of 2.8 km s^{-1} . Note that the stations azimuths (in degrees) are given to the right of the station names, and that the onset time of the source time functions is 1.0 s in this and subsequent figures. (b) Normalized variance for the two nodal planes over the complete velocity range. The thick line is the 165° plane and the thin line is the 257° plane. (c) The slip distribution at 2.8 km s^{-1} on the 165° plane. The average non-zero slip is 12 cm. (d) The error distribution of slip at 2.8 km s^{-1} on the 165° plane. The average non-zero error is 25–50 per cent of the average slip.

SLIP INVERSION

We adopt the slip inversion procedure of Mori & Hartzell (1990) and Mori (1993). The inversion solves for slip distribution on a given fault with a circular rupture front moving at a constant rupture velocity. The model fault is divided into a grid of subfaults centred at the hypocentre. We calculate synthetic source time functions for each subfault using a technique similar to QUAKE7 (Spudich & Frazer 1984). We use a rectangular grid rather than a triangular grid, however, and the directivity effects for the subfaults are calculated using a standard cosine directivity function rather than by numerical integration of rupture time isochrons. We use an 11×11 grid of subfaults in

each case, as this number of unknowns is reasonable for the available input data. We vary the size of the individual subfaults in the different events to obtain a fault dimension appropriate for the average duration of the source time functions and the size of the earthquake. The grid sizes and other input parameters to the inversion are given in Table 2. The waveforms are all normalized to unit area so as to give each station equal weight in the inversion.

The slip is calculated by least-squares inversion with a positivity constraint (Lawson & Hanson 1974). The fit of the data to the model is evaluated using the variance, which we normalize by the square of the maximum amplitude of the input data for each earthquake. The uncertainty in the slip on individual

Table 2. Input parameters for the slip inversion.

Event	Subfault size (m × m)	Depth to centre (km)	Nodal Plane 1		Nodal Plane 2		Moment (× 10 ¹⁴ N m)	Stress drop (MPa)
			Strike	Dip	Strike	Dip		
A	200 × 200	9.8	165°	83°	257°	75°	57	8 (20)*
B	100 × 100	5.5	150°	75°	242°	83°	0.87	3
C	200 × 200	4.1	158°	68°	253°	76°	2.8	1 (6)
D	100 × 100	9.1	149°	47°	45°	75°	2.2	9–12

*The stress drop for the principal subevent is given in brackets.

subfaults is estimated from the model covariance matrix and a data error estimate of 10 per cent (Mori & Hartzell 1990; Mori 1993).

We perform the inversion on both nodal planes for each focal mechanism, using a range of fixed rupture velocities. If one nodal plane consistently produces a better fit to the data then it can be interpreted as the fault plane. Rupture velocity is typically between about 60 and 90 per cent of the S wave velocity (β) (e.g. Dreger 1994a). At the hypocentral depth of

Events A and D, β is 3.5–3.6 km s⁻¹, and at the shallower depths of Events B and C, β is 3.2–3.4 km s⁻¹ (Abercrombie *et al.* 2000). We invert all four earthquakes by assuming rupture velocities between 2.0 and 3.6 km s⁻¹ at 0.1 km s⁻¹ intervals.

To estimate the actual values of slip, the seismic moment of the solution is set equal to the moment of the main shock (Table 2) calculated from the S -wave displacement spectral amplitudes (Brune 1970). To calculate the moment of the slip model, we assume that the rigidity is 3.5×10^{10} N m⁻².

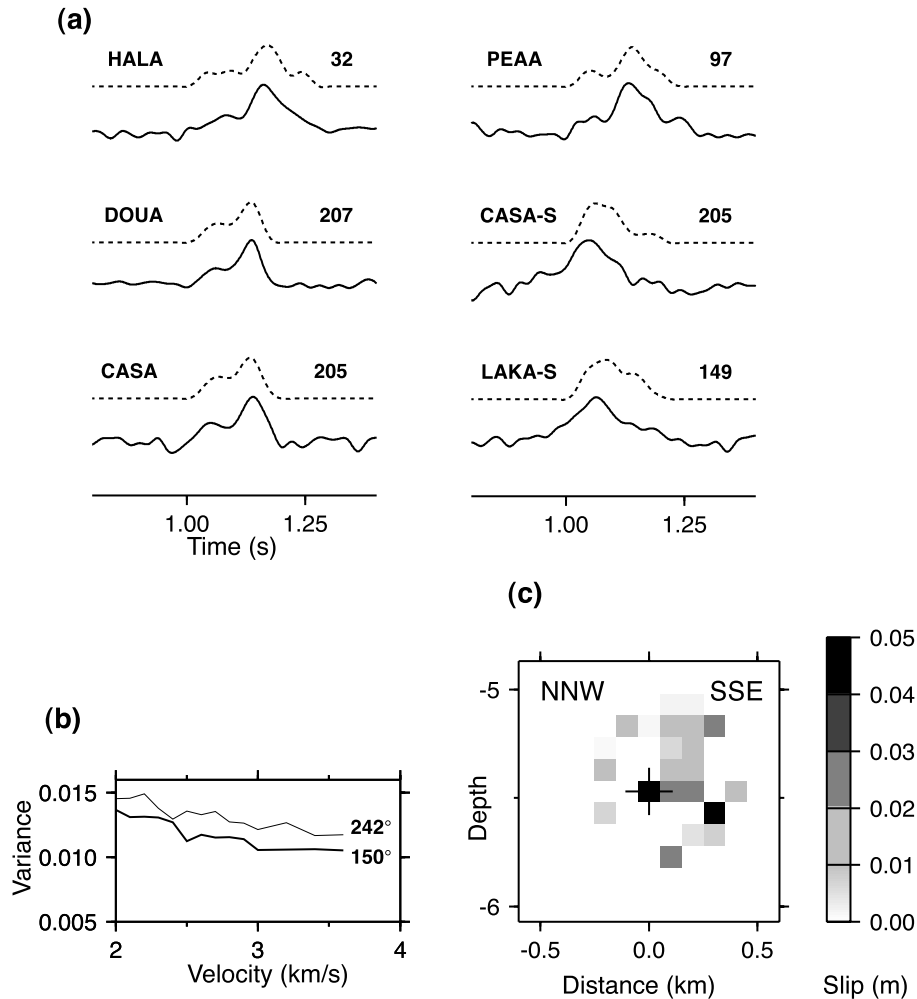


Figure 4. Event B (M_L 4.2): source time functions and slip inversion results. (a) Deconvolved source time functions input to the slip inversion (solid lines) and the synthetic seismograms from the best-fitting model (dashed lines) using the 150° plane and a rupture velocity of 2.6 km s⁻¹. (b) Normalized variance for the two nodal planes over the complete velocity range. The thick line is the 150° plane and the thin line is the 242° plane. (c) The slip distribution at 2.6 km s⁻¹ on the 150° plane. The average non-zero slip is 1.5 cm and the average error is about 50 per cent of this.

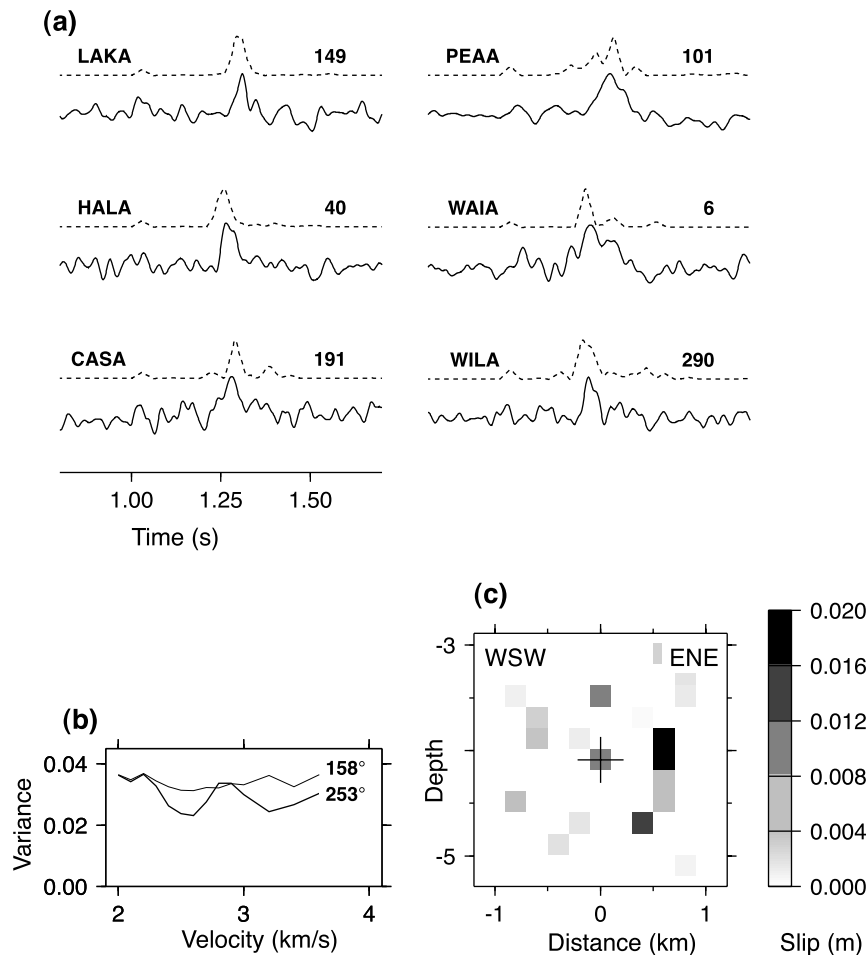


Figure 5. Event C (M_L 4.1): source time functions and slip inversion results. (a) Deconvolved source time functions input to the slip inversion (solid lines) and the synthetic seismograms from the best-fitting model (dashed lines) using the 253° plane and a rupture velocity of 2.5 km s^{-1} . Stations CASA and WAIA were given zero weight in the inversion because of their relatively high noise levels. (b) Normalized variance for the two nodal planes over the complete velocity range. The thick line is the 253° plane and the thin line is the 158° plane. (c) The slip distribution at 2.5 km s^{-1} on the 253° plane. The average non-zero slip is 2 cm and the average error is 25–50 per cent of this.

RESULTS

Event A (M_L 5.1)

The source time functions derived for Event A at stations WAIA and HALA to the north are longer than those from stations to the south (CASA and DOUA), which implies that rupture propagation is to the south (Fig. 3a). The inversion finds consistently better fits with the 165° nodal plane than the 257° nodal plane (Fig. 3b). We interpret the 165° plane as the fault plane, and therefore conclude that this earthquake did not rupture the Bruce fault but a conjugate fault.

The variance decreases with increasing velocity at low rupture velocities, and then is almost constant for both planes above about 2.4 km s^{-1} . At low velocities ($< 2.4 \text{ km s}^{-1}$) the model slip is not able to propagate far enough across the model fault plane to match the data well. Previous studies (e.g. Mori & Hartzell 1990; Mori 1993; Dreger 1994b) have found that slip inversions yield only a weak constraint on the rupture velocity. The variance is often observed to decrease with increasing velocity simply because the faster propagation enables more subfaults to rupture and so increases the number of free para-

meters (Mori & Hartzell 1990). The actual minimum variance reduction is thus not a reliable indicator of rupture velocity. A relatively simple distribution of slip that remains stable with small changes in rupture velocity is the most reliable indication of a good fit (Mori 1993). We therefore prefer a rupture velocity of 0.8β , which is a typical average, for all four earthquakes studied here. For Event A, 0.8β is 2.8 km s^{-1} ; the corresponding slip distribution is shown in Fig. 3(c) and the uncertainties in Fig. 3(d). The average non-zero slip is 12 cm and the average errors are 3–6 cm, about 50 per cent of the average slip. The slip distribution remains stable for the rupture velocities from 2.7 – 3.2 km s^{-1} . If the rupture area is equated to a circle, then the stress drop is about 8 MPa for the entire rupture and 20 MPa if only the principal region of slip is considered (Eshelby 1957).

Event B (M_L 4.2)

The source time functions of Event B are shorter at stations CASA and DOUA to the south than at HALA to the north (Fig. 4). Also, the waveform at PEEA is more similar to that of HALA than that of CASA, suggesting that it is on the same

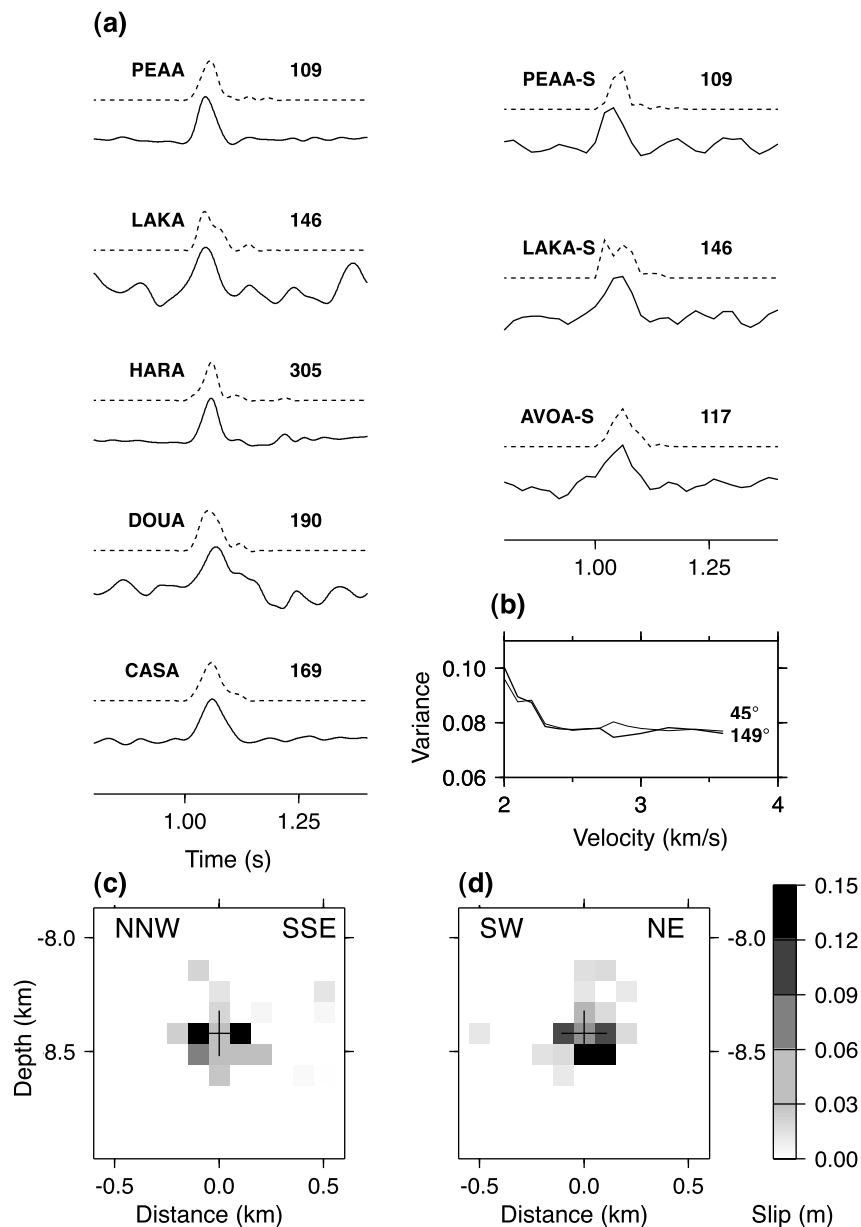


Figure 6. Event D (M_L 4.1): source time functions and slip inversion results. (a) Deconvolved source time functions input to the slip inversion (solid lines) and the synthetic seismograms from the model (dashed lines) using the 149° plane and a rupture velocity of 2.8 km s^{-1} . (b) Normalized variance for the two nodal planes over the complete velocity range. The thick line is the 149° plane and the thin line is the 45° plane. (c) The slip distribution at 2.8 km s^{-1} on the 149° plane. The average non-zero slip on both planes is 3.8 cm, and the average non-zero error is about 65 per cent of this. (d) The slip distribution at 2.8 km s^{-1} on the 45° plane.

side of the fault as HALA (Mori & Hartzell 1990). The slip inversion is consistently able to obtain a better fit to the data using the 150° plane, so we interpret this to be the fault plane. The variance of both planes (Fig. 4b) decreases with increasing velocity, reflecting the observed increase in the number of sub-faults ruptured as the rupture velocity is increased. A rupture velocity of 2.6 km s^{-1} is about 0.8β at the depth of Event B, and results in a concentration of slip up-dip and to the SSE of the hypocentre. Again, the slip distribution is relatively insensitive to moderate changes in rupture velocity. The average stress drop, including all the area that ruptured at 2.8 km s^{-1} , is about 3 MPa.

Event C (M_L 4.1)

This earthquake has the most complex source time functions (Fig. 5a). Only a small pulse can be discerned at the origin, followed by a much stronger one approximately 0.25 s later. We interpret these as an initial small subevent triggering the main slip. The large slip is probably displaced from the hypocentre because the timing of the largest peak varies from station to station. It arrives earliest at WAIA and WILA, next at HALA and last at PEAA and LAKA. We attempted a relative relocation of the two subevents, but the small amount of data and ambiguity of picking the onset of the second

subevent resulted in minimal constraints. The slip inversion is able to match the data significantly better using the 253° plane over most of the velocity range. A rupture velocity of 2.5 km s^{-1} corresponds to 0.8β at the hypocentre. The slip patterns on the 253° plane are relatively stable for small changes in the rupture velocity, and consistently show a small patch of slip at the hypocentre and a larger one at similar depth to the ENE. When using the 158° plane, the inversion is only able to match the waveforms by distributing the slip randomly around the slip plane. At velocities greater than 3 km s^{-1} the rupture front reaches the edge of the model fault grid by the end of the largest subevent. To ensure that our results are not being affected by the small grid size, we re-invert the data from this earthquake using a larger $300 \times 300 \text{ m}$ subfault size. The lower-resolution model cannot fit the waveforms as well, but the best fit is still for the 253° plane at a rupture velocity of about 2.5 km s^{-1} . This earthquake involved a small initial subevent at the hypocentre, followed by the largest subevent about 600 m ENE, at approximately the same depth. The average stress drop is about 1 MPa for the entire rupture area, and 6 MPa in the largest subevent, assuming the rupture velocity to be 2.5 km s^{-1} .

Event D (M_L 4.1)

Event D has the shortest, simplest source time functions, with an average duration of only about 0.1 s (Fig. 6a). Some azimuthal variation can be seen, with the pulse peaking earliest at PEAA and LAKA, and later at DOUA and CASA. The inversion variance is similar for both planes, however, and the slip patterns are simple and stable to small changes in rupture velocity (Figs 6b, c and d). The source time functions are so short that the slip is concentrated in the central nine subfaults even at rupture velocities nearing β . Decreasing the subfault size would not be worthwhile, as such high resolution requires higher frequencies than are present in the data. The average stress drops are about 9 and 12 MPa for the 45° and 149° nodal planes, respectively, assuming that the rupture velocity is 2.8 km s^{-1} (0.8β).

DISCUSSION AND CONCLUSIONS

We have determined the fault planes of three of the four earthquakes studied. The hypocentres are well constrained and the inversions are relatively insensitive to hypocentral errors since they do not use absolute times, and small and nodal arrivals are excluded. The orientations of the fault planes are subject to the same uncertainties as the original focal mechanisms, probably less than 15° (R. Robinson, personal communication, 2000). Such errors will produce uncertainties in the slip distributions. The good station distributions mean that these uncertainties should not affect our choice of fault plane.

Events A and B are the largest in a group of aftershocks located vertically beneath the mapped active trace of the Bruce fault, but they ruptured fault planes at a high angle to this fault. Hence, the Bruce fault cannot have slipped in an earthquake larger than about M_L 4. Event A was the only one of the four earthquakes studied that was large enough to have identifiable small aftershocks. These seven aftershocks occurred close to Event A within the following 30 min. They align roughly NW–SE, consistent with the 165° fault plane preferred by the slip inversion. The largest aftershock in the whole Arthur's Pass

sequence was located near the surface trace of the Harper fault, but probably did not rupture this fault but an unmapped conjugate (Abercrombie *et al.* 2000). Therefore, although alignments of aftershocks occurred along both the Bruce and Harper faults, in neither case did the largest of these aftershocks rupture the mapped faults.

Event C is located within a lineation of aftershocks striking parallel to the Bruce fault to the north. Unlike the other two earthquakes, the preferred rupture plane of this event (253°) is close to the regional mapped fault trend. This suggests that some slip occurred on an unmapped right-lateral strike-slip fault that was activated during the Arthur's Pass aftershock sequence.

Few measurements of the seismic moment of New Zealand earthquakes are available, so those obtained here significantly improve the calibration of the New Zealand M_L (Haines 1981). They yield $M_w \approx M_L - 0.7$. Global estimates of M_w for the larger earthquakes in the region are about 0.3 magnitude units smaller than M_L . Leitner *et al.* (2001) calculated moment tensors for four aftershocks of the nearby Cass earthquake and found that $M_w \approx M_L - 0.25$.

ACKNOWLEDGMENTS

We are grateful to P. McGinty for calculating focal mechanisms for the small events and to R. Robinson for calculating the induced stress orientations. We also thank B. Leitner for discussion concerning earthquake magnitudes, and for providing a preprint of her paper. Reviews by R. Robinson, R. Benites, D. Wald, J. Boatwright, S. Ward, M. Savage, P. Abercrombie and two anonymous reviewers improved the clarity of this manuscript. This study was funded by the Earthquake Commission and the Foundation for Research, Science and Technology, New Zealand. REA thanks Harvard University for use of their facilities during the final stages of this work. This is IGNS Publication Number 1586.

REFERENCES

- Abercrombie, R.E. & Leary, P.C., 1993. Source parameters of small earthquakes recorded at 2.5 km depth, Cajon Pass, Southern California: implications for earthquake scaling, *Geophys. Res. Lett.*, **20**, 1511–1514.
- Abercrombie, R.E., Webb, T.H., Robinson, R., McGinty, P.J., Mori, J.J. & Beavan, J., 2000. The enigma of the Arthur's Pass, New Zealand, earthquake 1: reconciling a variety of data for an unusual earthquake sequence, *J. geophys. Res.*, **105**, 16 119–16 137.
- Anderson, H., Webb, T. & Jackson, J., 1993. Focal mechanisms of large earthquakes in the South Island of New Zealand: implications for the accommodation of Pacific–Australia plate motion, *Geophys. J. Int.*, **115**, 1032–1054.
- Bruce, J.N., 1990. Tectonic stress and seismic shear waves from earthquakes, *J. geophys. Res.*, **75**, 4997–5009.
- Chamberlain, C.G., 1996. Seismic hazard from cross-faulting in North Canterbury: broader implications from the Arthur's Pass earthquake sequence of 18 June 1994, *MSc thesis*, University of Canterbury, New Zealand.
- Dreger, D.S., 1994a. Investigation of the rupture process of the 28 June, 1992 Landers earthquake utilizing TERRAScope, *Bull. seism. Soc. Am.*, **84**, 713–724.
- Dreger, D.S., 1994b. Empirical Green's function study of the January 17, 1994 Northridge, California earthquake, *Geophys. Res. Lett.*, **21**, 2633–2636.

- Dreger, D.S., Ritsema, J. & Pasyanos, M., 1995. Broadband analysis of the 21 September, 1993, Klamath Falls earthquake sequence, *Geophys. Res. Lett.*, **22**, 997–1000.
- Eshelby, J.D., 1957. The determination of the elastic field of an ellipsoidal inclusion and related problems, *Proc. R. Soc. Lond.*, **A241**, 376–396.
- Gledhill, K.R., Randall, M.J. & Chadwick, M.P., 1991. The EARSS digital seismograph: system description and field trials, *Bull. seism. Soc. Am.*, **81**, 1380–1390.
- Haines, A.J., 1981. A local magnitude scale for New Zealand earthquakes, *Bull. seism. Soc. Am.*, **71**, 275–294.
- Lawson, C.L. & Hanson, R.J., 1974. *Solving Least Squares Problems*, Prentice Hall, Englewood Cliffs, NJ.
- Leitner, B., Eberhart-Phillips, D., Anderson, H., Nabal, K. & J.L., 2001. A focused look at the Alpine fault, New Zealand: seismicity, focal mechanisms and stress observations, *J. geophys. Res.*, **106**, 2193–2220.
- Mori, J., 1993. Fault plane determinations for three small earthquakes along the San Jacinto fault, California: search for cross faults, *J. geophys. Res.*, **98**, 17 711–17 722.
- Mori, J., 1996. Rupture directivity and slip distribution of the M4.3 foreshock to the 1992 Joshua Tree earthquake, southern California, *Bull. seism. Soc. Am.*, **86**, 805–810.
- Mori, J. & Hartzell, S., 1990. Source inversion of the 1988 Upland, California, earthquake: determination of a fault plane for a small event, *Bull. seism. Soc. Am.*, **80**, 507–518.
- Robinson, R. & McGinty, P.J., 2000. The enigma of the Arthur's Pass, New Zealand, earthquake, 2: the aftershock distribution and its relation to regional and induced stress fields, *J. geophys. Res.*, **105**, 16 137–16 150.
- Spudich, P. & Frazer, L.N., 1984. Use of ray theory to calculate high-frequency radiation from earthquake sources having spatially variable rupture velocity and stress drop, *Bull. seism. Soc. Am.*, **74**, 2061–2082.